Extremely Low Thermal Conductivity and High Thermoelectric Performance in Liquid-like $Cu_2Se_{1-x}S_x$ Polymorphic Materials

Kunpeng Zhao[1,2], Anders Bank Blichfeld[3,4], Espen Eikeland[3,5], Pengfei Qiu[1], Dudi Ren[1], Bo Brummerstedt Iversen[3], Xun Shi[1*], and Lidong Chen[1*]*

1 State Key Laboratory of High Performance Ceramics and Superfine Microstructure, Shanghai Institute of Ceramics, Chinese Academy of Sciences, Shanghai 200050, China.

2 University of Chinese Academy of Sciences, Beijing 100049, China.

3 Centre for Materials Crystallography, Department of Chemistry and iNANO, Aarhus University, Langelandsgade 140, DK-8000 Aarhus C, Denmark.

4 Department of Materials Science and Engineering, Norwegian University of Science and Technology, N-7491 Trondheim, Norway.

5 Danish Technological Institute, Centre for Nano Production and Micro Analysis, DK-2630 Taastrup, Denmark.

Abstract

Recently, copper chalcogenides $Cu_{2-x}\delta$ (δ = S, Se, Te) have attracted great attentions due to their exceptional thermal and electrical transport properties. Besides those binary $Cu_{2-x}\delta$ compounds, the ternary $Cu_{2-x}\delta$ solid solutions are also expected to possess excellent thermoelectric performance. In this study, we have synthesized a series of $Cu_2Se_{1-x}S_x$ (x = 0.2, 0.3, 0.5, and 0.7) solid solutions by melting the raw elements followed by spark plasma sintering. The energy dispersive spectroscopy mapping, powder and single-crystal X-ray diffraction and X-Ray powder diffraction studies suggest that Cu_2Se and Cu_2S can form a continuous solid solution in the entire composition range. These $Cu_2Se_{1-x}S_x$ solid solutions are polymorph materials composed of varied phases with different proportions at room temperature, but single phase materials at elevated temperature. Increasing the sulfur content in $Cu_2Se_{1-x}S_x$ solid solutions can greatly reduce the carrier concentration, leading to much enhanced electrical resistivity and Seebeck coefficient in the whole temperature range as compared with those in binary Cu_2Se. In particular, introducing sulfur at Se-sites reduces the speed of sound. Combining the strengthened point defect scattering to phonons, extremely low lattice thermal conductivities are obtained in these solid solutions. Finally, a maximum zT value of 1.65 at 950 K is achieved for $Cu_2Se_{0.8}S_{0.2}$, which is greater than those of Cu_2Se and Cu_2S.

1. Introduction

Over the past decade, there has been a great interest in the field of thermoelectrics driven by the need for more efficient materials for solid state refrigeration and power generation.[1-7] The thermoelectric (TE) technology has many advantages over conventional refrigerators and power generators such as solid-state operation, compact design, vast scalability, zero-emissions, and long operating lifetime with no maintenance.[8] The conversion efficiency of a thermoelectric device is highly dependent on the thermoelectric Figure of merit, defined as $zT = \alpha^2 T/(\rho\kappa)$, where α is the Seebeck coefficient (thermopower), T is the absolute temperature, ρ is the electrical resistivity, and κ is the thermal conductivity. An ideal TE material should have excellent electrical transport properties (high α and low ρ) as well as poor thermal transport properties (low κ). However, α, ρ, and κ are usually correlated with each other in one material leading to the great difficultly and challenge to improve zT.[9]

Recently, the phonon-liquid electron-crystal (PLEC) concept has been proposed as a good extension of the phonon-glass electron-crystal (PGEC) concept to screen high performance TE materials by decoupling the correlation between electrical and thermal transports.[4, 10] The materials satisfying the PLEC concept are usually built up of a solid anion sublattice and a liquid-like cation sublattice.[11-15] The rigid anion sublattice provides a crystalline pathway for electrons transport, while the liquid-like cation sublattice can greatly scatter the heat-carrying phonons and even eliminate some of the transverse vibrational modes, leading to simultaneously shortened phonon mean free path and reduced heat capacity below the Dulong-Petit value at high temperatures.[11, 13] Motivated by the PLEC concept, many superionic compounds, such as $Cu_{2-x}\delta$ (δ = S, Se, Te),[11, 12, 16-20] CuAgSe,[21, 22] Cu_5FeS_4,[23] Ag/Cu-based chromium diselenides,[14, 24] and argyrodite-type compounds,[15] have been discovered with ultra-low thermal conductivity and high zT values. Among them, copper chalcogenides $Cu_{2-x}\delta$ (δ= S, Se, Te) have attracted great attentions due to their unique features of environmentally benign, low-cost, and earth-abundant. In spite of their simple chemical formulas, $Cu_{2-x}\delta$ materials have quite complex crystal structures.[25-29] For example, the crystal structure of the room temperature Cu_2Se phase is still controversial up to now, although recently an average structure of the compound has been determined.[25, 26, 29, 30] Upon heating, Cu_2Se undergoes a reversible phase transition at around 400 K and transforms to the superionic phase with high symmetry cubic structure (space group $Fm\bar{3}m$). Similar to Cu_2Se, the

stoichiometric Cu_2S compound also shows complicated temperature dependent structures, termed the monoclinic structure (for temperatures below 370 K), the superionic hexagonal structure (for temperatures between 370 K and 700 K), and the superionic cubic structure (for temperatures above 700 K).[27] In the case of Cu_2Te, the temperature-dependent phase transitions are even more complex, because it needs to go through five phase transitions to convert into the final superionic cubic phase.[31] Since 2012, the TE properties of $Cu_{2-x}\delta$ (δ = S, Se, Te) have been extensively studied. High *zT*s, 1.7-1.9 for Cu_2S,[12, 32] 1.5-1.8 for Cu_2Se,[11, 17, 33] and 1.1 for Cu_2Te,[20] have been reported for these binary copper chalcogenides.

Besides these binary materials, the investigation of copper chalcogenides $Cu_{2-x}\delta$ (δ = S, Se, Te) has already been extended to their ternary solid solutions.[34-36] He *et al.* successfully synthesized $Cu_2S_{0.5}Te_{0.5}$ solid solution with half-S and half-Te although Cu_2S and Cu_2Te have completely different crystal structures at room temperature.[35] Due to the large electronegativity and atomic size difference between S and Te, a unique mosaic structure is observed in $Cu_2S_{0.5}Te_{0.5}$ solid solution. This mosaic structure can introduce additional lattice strains or interfaces to strongly scatter phonons while scarcely affecting the electron transport, which results in an exceptional high *zT* around 2.0 at 1000 K. Most recently, our study showed that the $Cu_2S_{0.5}Se_{0.5}$ solid solution with half-S and half-Se can be also synthesized, which has a unique hierarchical microstructure composed of mesoscale polymorphs, nanoscale domains, and modulations.[36] However, so far, the TE properties of ternary $Cu_2Se_{1-x}S_x$ solid solutions with other S/Se atomic ratio have not been reported. In the present study, we further synthesized a series of $Cu_2Se_{1-x}S_x$ (x = 0.2, 0.3, 0.5, 0.7) solid solutions with different S/Se atomic ratios. Their phase compositions, crystal structures, microstructure, and electrical and thermal properties have been systematically investigated. The evolution of TE properties as a function of the sulfur alloying content has been deeply analyzed and the relevant mechanisms have been discussed.

2. Experimental Section

2.1 Synthesis. Polycrystalline $Cu_2Se_{1-x}S_x$ (x = 0.2, 0.3, 0.5, and 0.7) samples were synthesized by a combination of melting and long-term high-temperature annealing. High purity raw elements, Cu (shot, 99.999%, Alfa Aesar), Se (shot, 99.999%, Alfa Aesar), and S (shots, 99.9999%, Alfa Aesar) were combined in their stoichiometric ratios and placed in Boron Nitride

crucibles, which were then sealed in a fused silica tube under vacuum. The tubes were slowly (100 K h^{-1}) raised to 1423 K and stayed at that temperature for 12 h, and then cooled down to 1073 K in 24 h. After annealing at 1073 K for 8 days, the tubes were furnace cooled to room temperature. Small single crystals were extracted from the polycrystalline ingot sample after the annealing process. Finally, the annealed ingots were crushed into powders and consolidated by spark plasma sintering (Sumitomo SPS-2040) at 873 K under a pressure of 65 MPa for 5 minutes. Electrically insulating and thermally conducting BN layers were sprayed onto the carbon foils and the inner sides of the graphite die before the SPS process in order to prohibit DC pulsed currents going through the powders.

2.2 Characterization. Single-crystal (about 10 × 40 × 60 μm^3) X-ray diffraction (SCXRD) measurements were performed on a SuperNova diffractometer from Agilent Technologies using $Mo_{K\alpha}$ radiation (λ= 0.71073 Å). Diffracted intensities were collected on a CCD detector and the data were integrated and corrected for absorption using CrysAlisPro. The structure solution and refinement were carried out with SHELXT, using the Olex2 gui. Room temperature powder X-ray diffraction (RT-PXRD) data were collected at the beam line BL02B2 at SPring-8, Japan.[37] Full profile refinements by Rietveld analysis were carried out for $Cu_2Se_{1-x}S_x$ samples using the program MAUD. High-temperature powder X-ray diffraction (HT-PXRD) measurements were carried out on a Rigaku Smartlab with a 9 kW rotating Co K_α source and parallel beam optics and equipped with an Anton-Paar Domed Hot Stage sample environment. The sample morphologies were measured by field emission scanning electron microscopy (FESEM, Magellan-400). The sound speed data were obtained by use of ultrasonic measurement system UMS-100 with shear wave transducers of 5 MHz and longitudinal wave transducers of 10 MHz. The electrical resistivity (ρ) and Seebeck coefficient (α) were simultaneously obtained on a commercial system (ULVAC ZEM-3). Thermal diffusivity (D) was measured using the laser flash method (Netzsch, LFA-457). The specific heat (C_p) was determined by differential scanning calorimetric using Netzsch DSC 404F3. The densities (d) were measured by the Archimedes method. The total thermal conductivity (κ) was calculated according to the relationship $\kappa = dC_pD$. Uncertainties in the electrical conductivity, Seebeck coefficient, and thermal conductivity were within 5%, 7%, and 5%, respectively. The Hall coefficient (R_H) at 300 K was measured using a physical properties measurement system (PPMS-9, Quantum Design, USA) with a magnetic field from -3 to 3 T. The

hole concentration (p) was calculated using $p = 1/(R_H e)$, where e is the elementary charge. Hall carrier mobility (μ_H) was calculated according to the relation $\mu_H = R_H/\rho$.

3. Results and Discussion

3.1 Phase composition and crystal structure

The phase compositions of the synthesized $Cu_2Se_{1-x}S_x$ samples are characterized by the energy dispersive spectroscopy (EDS). Take $Cu_2Se_{0.8}S_{0.2}$ sample as an example, Fig. 1a shows that all elements (Cu, Se, and S) are homogenously distributed throughout the target phase region. No element enrichment is observed. However, the electron backscatter diffraction (EBSD) measurement (Fig. 1b) performed in a local area (25 μm × 20 μm) suggests that the $Cu_2Se_{0.8}S_{0.2}$ sample is not a simple single phase at room temperature. Three different phases are detected, which are identified as the hexagonal, cubic, and trigonal phases, respectively. Combining the homogeneous element distribution, it is concluded that these phases have very close or even identical chemical compositions but different crystal structures, agreeing well with the concept of polymorphism.[26, 38]

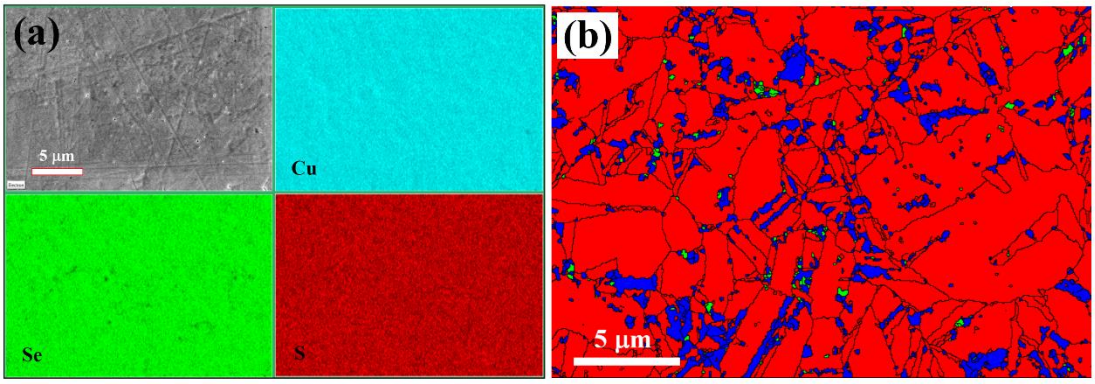

Fig. 1. (a) Secondary electron (SE) image and elemental energy dispersive spectroscopy (EDS) mapping for $Cu_2Se_{0.8}S_{0.2}$. **(b)** Phase map of $Cu_2Se_{0.8}S_{0.2}$ obtained from electron backscatter diffraction (EBSD) measurement. The red, blue and green grains are identified as hexagonal phases, cubic phases, and trigonal phases, respectively. The ratios of different phases shown in the phase map are just for reference because the small grains below the step size of EBSD (150nm) are ignored during the measurement. The real contents can be obtained by the X-ray Rietveld refinement and given in Table 1.

To further analyze the polymorphic feature of these $Cu_2Se_{1-x}S_x$ materials, synchrotron powder X-ray diffraction data were collected at room temperature. As shown in Fig. 2a and Fig. S1†, the diffraction patterns for $Cu_2Se_{1-x}S_x$ are quite different compared with those of the binary phases Cu_2Se and Cu_2S. In the sample $Cu_2Se_{0.8}S_{0.2}$, besides those diffraction peaks indexed by the hexagonal structure (ICSD-95397), some weak diffraction peaks identified as the $Fm\bar{3}m$ cubic structure (ICSD-54916) and trigonal phase (ICSD-4321181) are also identified. This agrees well with the EBSD measurements shown above that sample $Cu_2Se_{0.8}S_{0.2}$ is a polymorph material at room temperature. However, in samples $Cu_2Se_{1-x}S_x$ (x = 0.3 and 0.5), only the diffraction peaks belonging to the hexagonal phase and cubic phase are observed while those belonging to the trigonal phase disappear. Furthermore, in $Cu_2Se_{0.3}S_{0.7}$, only the hexagonal phase remains. Based on the X-ray diffraction patterns, the volume fractions of each phase are calculated by Rietveld refinement for each sample. The results are shown in Fig. 2b. In $Cu_2Se_{0.8}S_{0.2}$, the volume fractions of the hexagonal phase, cubic phase, and trigonal phase are 41.3%, 55.1%, and 3.6%, respectively. With increasing the sulfur content to 0.3 and 0.5, the volume fraction of cubic phase is gradually decreased. When the sulfur content reaches 0.7, the cubic phase completely disappears and the volume fraction of the hexagonal phase is 100%.

Based on the room temperature powder X-ray diffraction (PXRD) data, the lattice parameters for hexagonal and cubic phases are refined. The results are shown in Fig. 2c and d. Because of the smaller atomic size of S (1.04 Å) than that of Se (1.17 Å), the substitution of S at Se-site in $Cu_2Se_{1-x}S_x$ should decrease the lattice parameters according to the Vegard's law, which is consistent with those experimental data shown in Fig. 2c and d. Combining the homogeneously distributed elements in $Cu_2Se_{1-x}S_x$ samples (see Fig. 1a and b), the present results prove that the $Cu_2Se_{1-x}S_x$ samples are still ideal solid solutions although they consist of varied phases depending on the S alloying content.

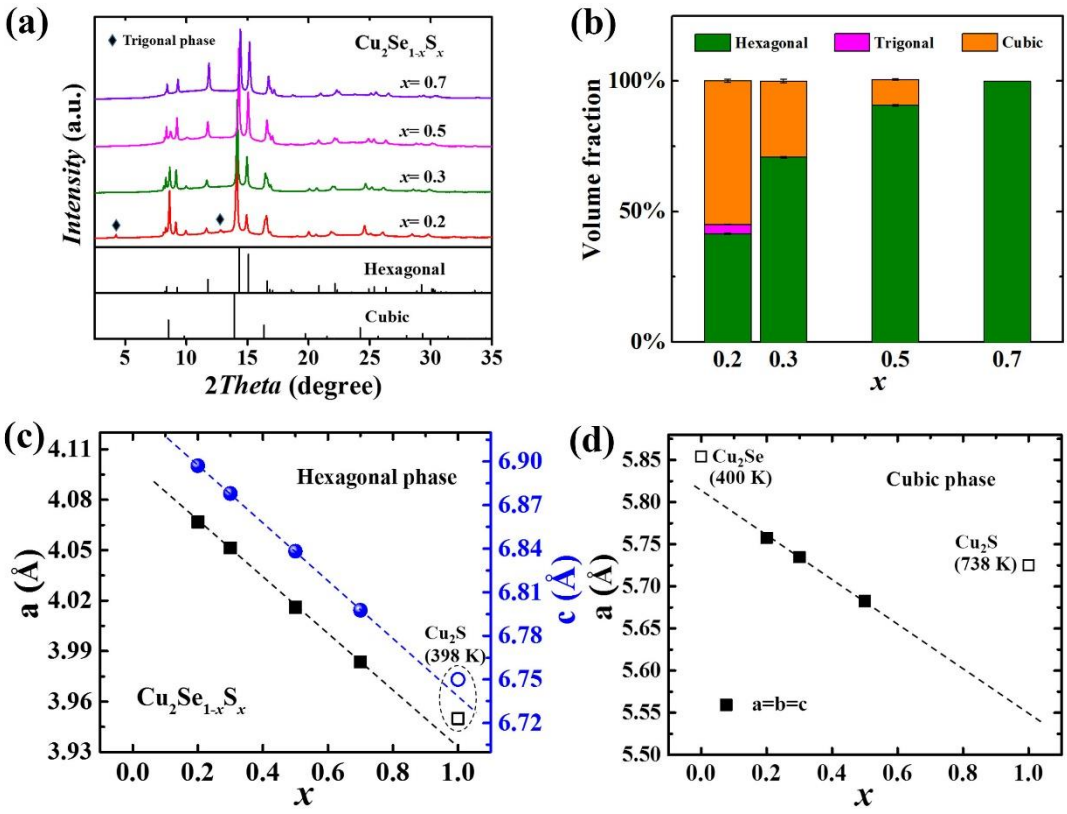

Fig. 2. **(a)** Synchrotron powder X-ray diffraction patterns measured by a wavelength of 0.5001652(14) Å for $Cu_2Se_{1-x}S_x$ (x = 0.2, 0.3, 0.5, 0.7) at room temperature. **(b)** Volume fraction of each phase in $Cu_2Se_{1-x}S_x$. Sulfur content dependences of lattice parameters obtained by structural Rietveld refinement on the **(c)** hexagonal phase and **(d)** cubic phase in $Cu_2Se_{1-x}S_x$, with the statistical errors smaller than the data markers. The lattice parameters of hexagonal Cu_2S phase at 398 K are included in (c),[27] and those for cubic Cu_2S phase at 738 K and cubic Cu_2Se phase at 400 K are included in (d).[27, 29] They deviate from the trend for the $Cu_2Se_{1-x}S_x$ solid solutions due to the thermal expansions at high temperatures.

Table 1. Refined parameters and quality factors based on the PXRD data for $Cu_2Se_{1-x}S_x$ (x= 0.2, 0.3, 0.5, 0.7) at room temperature.

Sample	Phase	Fraction (vol%)	Space group	R_p (%)	R_{wp} (%)	χ^2
$Cu_2Se_{0.8}S_{0.2}$	Hexagonal	41.3(3)	$P6_3/mmc$	1.433	2.085	2.325
	Cubic	55.1(8)	$Fm\bar{3}m$			
	Trigonal	3.6(4)	$R\bar{3}m$			
$Cu_2Se_{0.7}S_{0.3}$	Hexagonal	70.8(3)	$P6_3/mmc$	1.458	2.261	2.443

	Cubic	29.2(1)	$Fm\bar{3}m$			
$Cu_2Se_{0.5}S_{0.5}$	Hexagonal	90.7(2)	$P6_3/mmc$	0.992	1.511	1.867
	Cubic	9.3(5)	$Fm\bar{3}m$			
$Cu_2Se_{0.3}S_{0.7}$	Hexagonal	100	$P6_3/mmc$	1.458	2.261	2.443

The crystal structures of the trigonal phase and cubic phase determined in these $Cu_2Se_{1-x}S_x$ solid solutions are the same as the room temperature Cu_2Se phase and the high temperature Cu_2Se superionic phase, respectively.[29, 39] Their crystal structures are shown in Fig. 3a and 3b. In this study, we used the single-crystal X-ray diffraction (SCXRD) measurements to clarify the detailed atomic occupations of the hexagonal structures in $Cu_2Se_{1-x}S_x$ (x = 0.2, 0.3, 0.5, 0.7) samples. The SCXRD data were collected at 100 K to ensure better diffraction data quality since the thermal vibration (dynamic disorder) is weak at low temperatures. Small single crystals with size of around 10 × 40 × 60 μm^3 were extracted from the polycrystalline sample cooled down from the melt. Taking $Cu_2Se_{0.8}S_{0.2}$ as an example, Se and S are randomly located at the same Wyckoff sites with the Se/S ratio of 4:1, as shown in Fig. 3c. These Se/S atoms form a rigid hexagonal framework, which is similar with that of the hexagonal Cu_2S structure. In addition, two different kinds of copper (Cu1: 2*b* & Cu2: 12*k*) Wyckoff sites are determined inside the crystal structure. The Cu1 site situates on the faces of the red octahedron shown in Fig. 3b, while the Cu2 site is located close to the center of the blue tetrahedron (see Fig. 3c), disordered about the 6_3-screw axis. The Se/S sites are fully occupied, while the Cu1 and Cu2 sites are partially occupied. This kind of crystal structure can well satisfy the PLEC concept mentioned above, in which the Cu ions can easily hop (flow) among different symmetry equivalent sites inside the rigid Se/S anion framework.[11, 15]

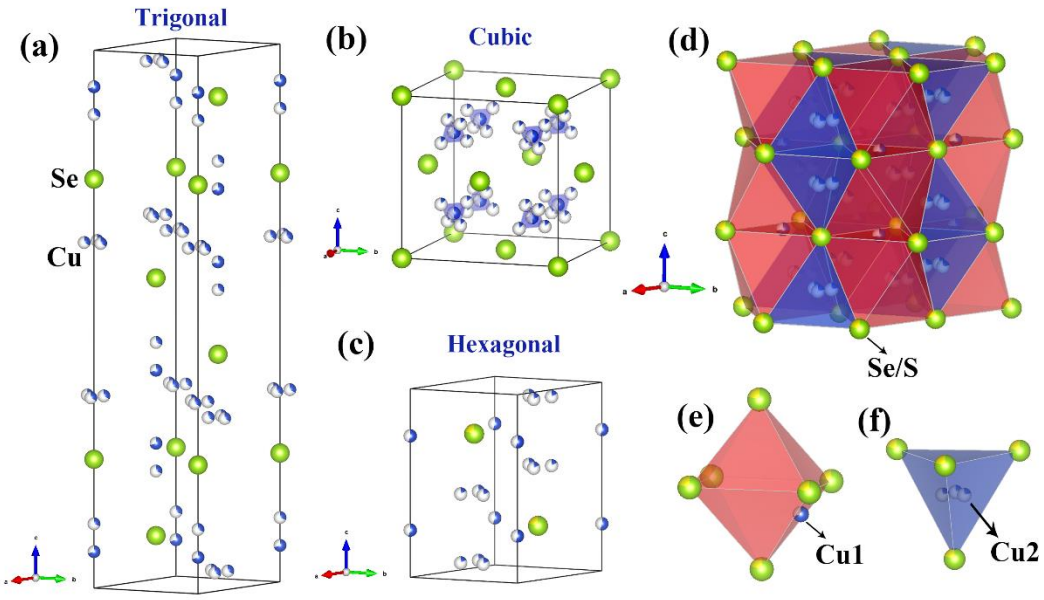

Fig. 3. Crystal structures of **(a)** trigonal phase, **(b)** cubic phase, and **(c)** hexagonal phase detected in the $Cu_2Se_{1-x}S_x$ solid solutions. **(d)** Visualization of the crystal structure of hexagonal phase ($P6_3/mmc$). **(e)** Red octahedron with Cu1 situated on one of the faces. **(f)** Blue tetrahedron with three Cu2 sites located inside. The atomic site occupancy is indicated by partial coloring of the atoms.

3.2 Phase transition character

Fig. 4 plots the measured heat capacity (C_p) curves for all $Cu_2Se_{1-x}S_x$ (x = 0.2, 0.3, 0.5, 0.7) solid solutions. The data of Cu_2Se and Cu_2S are also included for comparison.[11, 12] The stoichiometric Cu_2Se has one phase transition at around 400 K, while Cu_2S has two phase transitions, termed the monoclinic-hexagonal transition at around 370 K and the hexagonal-cubic transition at 710 K. Interestingly, the C_p curves for all $Cu_2Se_{1-x}S_x$ solid solutions are different from that for either Cu_2Se or Cu_2S, suggesting that the coexistence of S and Se in the anion sublattice not only alters the crystal structure but also changes the initial phase transition characters of binary Cu_2Se and Cu_2S. The C_p curve of $Cu_2Se_{0.8}S_{0.2}$ sample has two endothermic peaks. Combining the high temperature powder X-ray diffraction patterns (see Fig. 4b and Fig. S2†) for $Cu_2Se_{0.8}S_{0.2}$, the small peak at 347 K should be attributed to the phase transition from trigonal phase to hexagonal phase and the strong peak at 533 K should be attributed to the phase transition from hexagonal phase to cubic phase. Since there is no trigonal phase in the other $Cu_2Se_{1-x}S_x$ (x = 0.3, 0.5, 0.7) solid solutions at room temperature, their DSC curves only have one strong endothermic peak,

corresponding to the phase transition from the hexagonal phase to the cubic phase. With increasing the sulfur alloying content in $Cu_2Se_{1-x}S_x$ solid solutions, the temperature of this hexagonal–cubic phase transition gradually shifts to higher temperatures.

Interestingly, although the C_p peak appears around 500 K for $Cu_2Se_{0.8}S_{0.2}$, Fig. 4b shows that the intensities of those X-ray diffraction peaks belonging to cubic phase are gradually increased from 300 K to 500 K, while those belonging to hexagonal phase are gradually reduced as is corroborated by Rietveld analysis on the HT XRD data. More detailed information can be found in Table S1†. The $Cu_2Se_{0.8}S_{0.2}$ hexagonal phase and $Cu_2Se_{0.8}S_{0.2}$ cubic phase should have close formation enthalpies. A small external energy can trigger the phase transformation from the hexagonal phase to the cubic phase, and thus contribute extra energy to the C_p measurements. This can well account for the higher C_p values before the hexagonal–cubic phase transition than the Dulong-Petit value ($3Nk_B$) derived for typical solids. After the hexagonal–cubic phase transition, the C_p values decrease with increasing temperature. At elevated temperature, the C_p values are already approaching or even below the Dulong-Petit value ($3Nk_B$) (see Fig. 4a). This well proves the existence of liquid-like Cu ions inside these solid solutions, which can eliminate some of the vibrational modes and reduce the heat capacity. Thus, being similar with Cu_2Se or Cu_2S, extremely low lattice thermal conductivities are also expected in these $Cu_2Se_{1-x}S_x$ solid solutions.

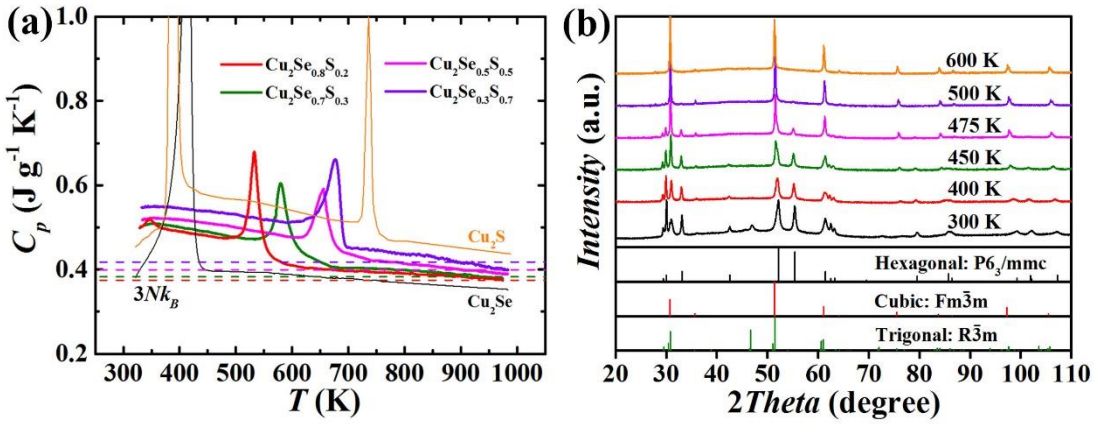

Fig. 4. (a) Temperature dependence of the heat capacity (C_p) for $Cu_2Se_{1-x}S_x$ (x = 0.2, 0.3, 0.5 and 0.7) solid solutions at constant pressure. The dashed lines represent the Dulong-Petit values ($3Nk_B$) at constant volume (C_v) in typical solids. The data of Cu_2Se and Cu_2S taken from Ref.11, 12 are included for comparison. **(b)** High temperature powder X-ray diffraction patterns for $Cu_2Se_{0.8}S_{0.2}$ measured from 300 K to 600 K.

3.3 Thermoelectric properties

The temperature dependent TE properties of $Cu_2Se_{1-x}S_x$ (x = 0.2, 0.3, 0.5, 0.7) solid solutions are shown in Fig. 5. The previously reported data of Cu_2Se and Cu_2S are also included for comparison.[11, 12] The $Cu_2Se_{1-x}S_x$ solid solutions are slightly anisotropic below the phase transitions at 510-730 K but isotropic above the phase transitions. At room temperature, the electrical resistivities ρ of all $Cu_2Se_{1-x}S_x$ samples range from 5×10^{-4} to 3×10^{-2} Ω m. These values are much higher than that of Cu_2Se. Some of them are even greater than that of Cu_2S. Owing to the presence of several different phases, the electrical resistivities of $Cu_2Se_{1-x}S_x$ show complicate temperature dependencies below 700 K. However, above 700 K, all $Cu_2Se_{1-x}S_x$ solutions convert to the cubic phase and their ρ values monotonously increase with increasing the sulfur alloying content. In addition, all $Cu_2Se_{1-x}S_x$ solid solutions possess much higher Seebeck coefficient α than Cu_2Se. At room temperature, the α of $Cu_2Se_{0.8}S_{0.2}$ is as high as 540 μV K^{-1}, about six times of that for Cu_2Se. Similar to the variation of ρ, the Seebeck coefficients of $Cu_2Se_{1-x}S_x$ samples do not show any monotonic increase or decrease at low temperatures. Until all the solid solutions convert to the cubic phase above 700 K, their α values start to show nearly monotonously variation with increasing the sulfur alloying content. Based on the measured ρ and α, the power factors ($PF = \alpha^2/\rho$) for $Cu_2Se_{1-x}S_x$ are calculated and shown in Fig. 5c. Obviously, all samples show two kinds of different temperature dependencies from 300 to 1000 K. The *PF*s for all $Cu_2Se_{1-x}S_x$ samples before the hexagonal-cubic phase transition are rather small with values of around 1 μW cm^{-1} K^{-2}, which are lower than those of both Cu_2Se and Cu_2S. However, after the hexagonal-cubic phase transition, the *PF*s for $Cu_2Se_{1-x}S_x$ samples are greatly improved. For instance, the maximum *PF*s of 8.4 μW cm^{-1} K^{-2} at 800 K and 4.3 μW cm^{-1} K^{-2} at 1000 K are obtained for $Cu_2Se_{0.8}S_{0.2}$ and $Cu_2Se_{0.3}S_{0.7}$, respectively. Furthermore, as a result of the enhanced ρ and α values, their *PF* values show a monotonously decrease with increasing the sulfur content after the hexagonal-cubic phase transition. Taking $Cu_2Se_{0.8}S_{0.2}$ as an example, up to 850 K, $Cu_2Se_{0.8}S_{0.2}$ exhibits good repeatability in electrical transports during the cycling processes (see Fig. S5).

Fig. 5d presents the temperature dependence of total thermal conductivity κ for $Cu_2Se_{1-x}S_x$. Interestingly, being different with the variations of ρ and α mentioned above, κ shows an almost independent dependency with the sulfur content. All solid solutions possess very low κ values around 0.2-0.4 W m^{-1} K^{-1} throughout the whole measured temperature range, which are

comparable with those of Cu_2S but much lower than those of Cu_2Se. The lattice thermal conductivity (κ_L) is calculated using the expression $\kappa_L = \kappa - \kappa_c$, in which the carrier thermal conductivity component (κ_c) is estimated using the Wiedeman-Franz law ($\kappa_c = LT/\rho$, where L is the Lorenz number). In this study, the L values are calculated according to ref. 40, 41

$$L = \left(\frac{k_B}{e}\right)^2 \left\{\frac{(\lambda+3)F_{\lambda+2}(\eta)}{(\lambda+1)F_{\lambda}(\eta)} - \left[\frac{(\lambda+2)F_{\lambda+1}(\eta)}{(\lambda+1)F_{\lambda}(\eta)}\right]^2\right\} \quad , (1)$$

where k_B is the Boltzmann constant, e is the electron charge, λ is the scattering factor, η ($=E_F/(k_BT)$) is the reduced Fermi energy. The Fermi integrals are given by $F_m(\eta) = \int_0^\infty \frac{x^m dx}{1+\exp(x-\eta)}$, where x is the reduced carrier energy. The calculated L values are shown in Fig. S3†. Because of the high electrical resistivities in $Cu_2Se_{1-x}S_x$, the contribution from the carriers to the total thermal conductivity is very small and thus κ_L is almost the same as κ. As shown in Fig. 5e, the κ_L of all samples show a weak temperature dependent behavior, which is also a common phenomenon in liquid-like materials.[11, 13] In the whole experimental temperature range, the κ_L values for all $Cu_2Se_{1-x}S_x$ samples are no more than 0.4 W m^{-1} K^{-1}, which are even below that for a glass.

The temperature dependent TE Figure of merit zT ($=\alpha^2T/(\rho\kappa)$) is shown in Fig. 5f. Similar to the PF variation, the zT of each $Cu_2Se_{1-x}S_x$ solid solution also shows two different trends that are separated by the hexagonal-cubic phase transition. Despite of the fairly low κ, the zT values at low temperatures are rather small due to the poor electrical transport properties. Nevertheless, the zT values are greatly improved after their respective phase transitions, mainly attributed by the improved power factors. A maximum zT value of 1.65 at 950 K is achieved for $Cu_2Se_{0.8}S_{0.2}$, which is comparable with that of Cu_2Se. If the electrical transports can be further improved in these solid solutions, higher zTs can be expected.

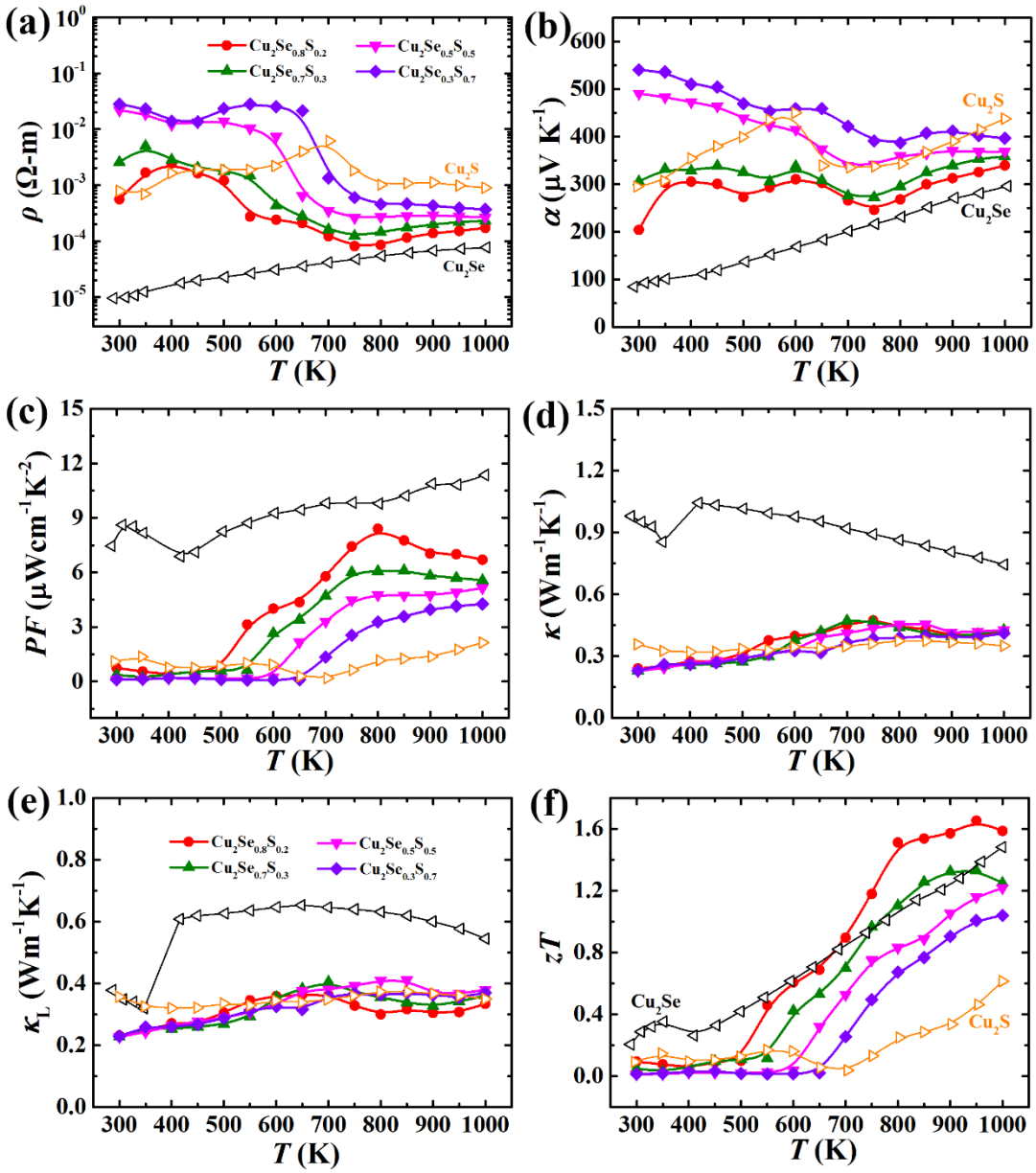

Fig. 5. Temperature dependency of **(a)** electrical resistivity ρ, **(b)** Seebeck coefficient α, **(c)** power factor PF, **(d)** total thermal conductivity κ, **(e)** lattice thermal conductivity κ_L, and **(f)** TE Figure of merit zT for $Cu_2Se_{1-x}S_x$ (x = 0.2, 0.3, 0.5 and 0.7) solid solutions. The data of Cu_2Se and Cu_2S taken from Ref. 11, 12 are also included for comparison.

To further illustrate the effect of sulfur alloying on electrical transport properties, we measured the room temperature Hall coefficient and then calculated the Hall carrier concentration p and mobility μ_H for all samples. The positive Hall coefficient confirms that holes are the majority carriers in $Cu_2Se_{1-x}S_x$, resulting from the nature of copper vacancies inside the crystal structure. Since the chemical bonds in Cu_2Se are relative weak, its p value is much higher than

that of Cu_2S. As shown in Fig. 6a, the p value of Cu_2Se is around 4.8×10^{20} cm^{-3}, which is about two orders of magnitude larger than that of Cu_2S. When increasing the sulfur alloying content in Cu_2Se solid solutions, p is firstly significantly decreased and followed by an increase. The lowest value of 1×10^{18} cm^{-3} is attained for the $Cu_2Se_{0.3}S_{0.7}$ sample. Such carrier concentration variation might be caused by the coexistence of multiple phases with different crystal structures and thus varied chemical bonds between Cu and Se/S. The carrier mobility μ_H as a function of sulfur content is presented in Fig. 6b. Here the μ_H data show a similar variation trend with p, which is mainly ascribed to the additional potential energy fluctuation due to the atomic level disorder introduced by S-alloying. Attributed by the simultaneously reduction of p and μ_H, the room temperature resistivity of $Cu_2Se_{1-x}S_x$ solid solutions are greatly increased. The largest ρ value of 3×10^{-2} Ω m is obtained for $Cu_2Se_{0.3}S_{0.7}$, which is almost three orders higher than that of Cu_2Se and one order larger than that of Cu_2S (see Fig. 6c). The Pisarenko relation, *i.e.* a plot of the Seebeck coefficient as a function of the carrier concentration, gives a good description of the experimental α results. As shown in Fig. 6d, the experimental data for all samples roughly fall on the theoretical line with the effective mass of 1.3 m_e, implying that all the $Cu_2Se_{1-x}S_x$ solid solutions have similar band structure near the Fermi level. Based on the single parabolic band (SPB) model, the optimum carrier concentration for both binary Cu_2Se and Cu_2S are in the order of 10^{20} -10^{21} cm^{-3} at high temperature.[12, 42] Therefore, the present low carrier concentrations provide a rather broad room to further optimize the electrical transport properties of these $Cu_2Se_{1-x}S_x$ solid solutions.

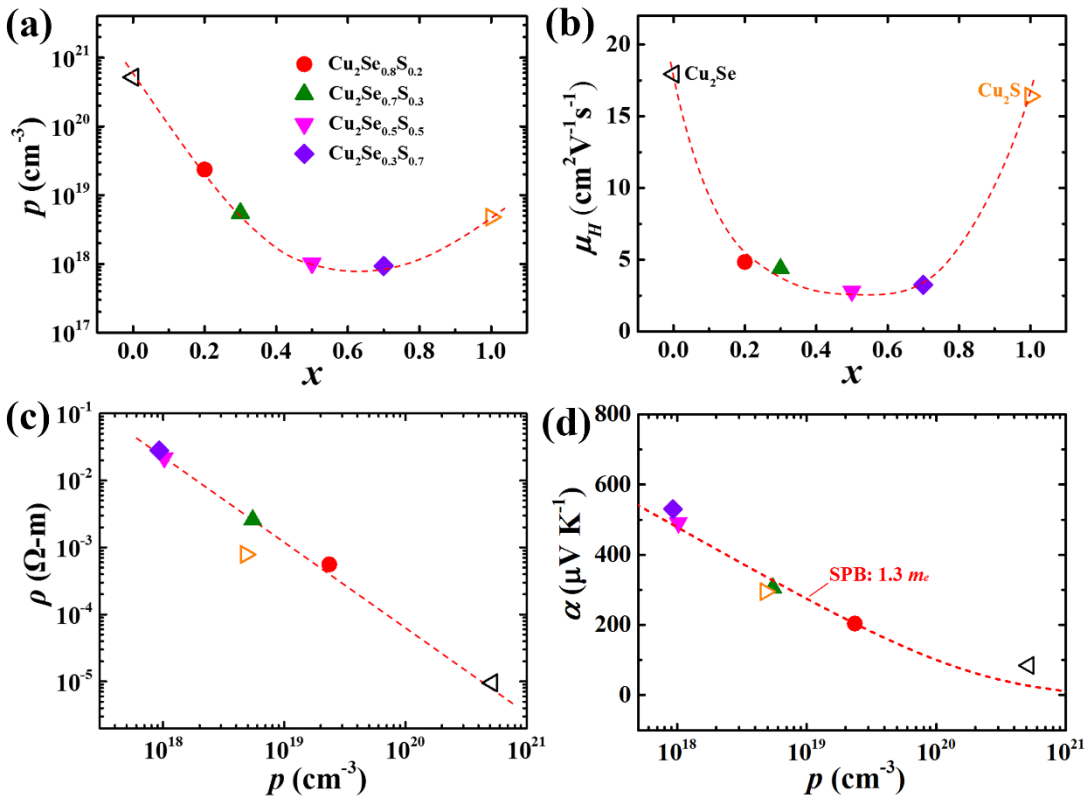

Fig. 6. Electrical transport properties of $Cu_2Se_{1-x}S_x$ (x = 0.2, 0.3, 0.5 and 0.7) solid solutions at 300 K. **(a)** Hole carrier concentration p and **(b)** carrier mobility μ_H as a function of sulfur content x. **(c)** Electrical resistivity ρ and **(d)** Seebeck coefficient α as a function of carrier concentration at 300 K. The dashed lines in (a, b, c) are guide to the eyes, and the dashed curve in (d) is the Pisarenko plot calculated from the single parabolic band (SPB) model. The data of Cu_2Se and Cu_2S taken from Ref. 11,12 are also included for comparison.

Fig. 7a shows the lattice thermal conductivity κ_L as a function of sulfur content x for all $Cu_2Se_{1-x}S_x$ solid solutions at 300 K. Obviously, the κ_L values for $Cu_2Se_{1-x}S_x$ solid solutions are smaller than those of both Cu_2Se and Cu_2S. Generally, κ_L can be given as $\kappa_L = v_{avg}\, C_V\, l/3$, where v_{avg}, C_V, and l are the average speed of sound, heat capacity, and phonon mean free path, respectively. We firstly measured the longitudinal v_l and transverse v_t speed of sound for all samples at room temperature. Surprisingly, we find the v_l values of $Cu_2Se_{1-x}S_x$ solid solutions are nearly the same as that of Cu_2Se, while the v_t values are significantly lower than those of both Cu_2Se and Cu_2S matrix. At room temperature, these solid solutions already partly or even completely crystalize in the superionic hexgonal or cubic phase, whereas Cu_2Se and Cu_2S are still

in the nomal phase. The melt-like copper sub-lattice in the $Cu_2Se_{1-x}S_x$ solid solutions can soften the shear modes,[11] leading to the low v_t shown in Fig. 7b. Similar case has been also observed in Cu_7PSe_6 superionic conductor.[13] Based on the measured v_l and v_t, we calculated the average speeds of sound v_{avg} ($= \left(\frac{2}{3v_t^3} + \frac{1}{3v_l^3}\right)^{-\frac{1}{3}}$) for all $Cu_2Se_{1-x}S_x$ solid solutions and plotted them in Fig. 7b. Clearly, the lowered v_{avg} is one reason for the abnormal low lattice thermal conductivity observed in these $Cu_2Se_{1-x}S_x$ solid solutions.

Besides the speeds of sound, alloying sulfur at Se sites can also change the phonon mean free path l by introducing additional mass and strain fluctuations to scatter phonons. In order to clarify this effect, we firstly normalize the lattice thermal conductivities of all $Cu_2Se_{1-x}S_x$ solid solutions by using the same v_{avg} with the Cu_2Se sample based on the equation of $\kappa_L = v_{avg}\, C_V\, l/3$. In this way, the contribution from the lowered speeds of sound in the total lattice thermal conductivities can be removed. Then, the Callaway model is used to interpret the normalized lattice thermal conductivities (open circles in Fig. 7a). In a solid solution, the lattice thermal conductivity is given by[43, 44]

$$\kappa_L = k_B/\left[4\pi v_s (ACT)^{1/2}\right] \quad , (2)$$

where CT is the relaxation time for phonon-phonon scattering (C is a constant and T is the temperature), v_s is the mean sound velocity and A is the coefficient for the Rayleigh-type point defect scattering rate. If we assume that Cu_2Se is a phase pure system, CT can be determined by

$$\kappa_{pure} = k_B^2 \Theta_D/[2\pi^2 v_s \hbar CT] \quad , (3)$$

where Θ_D is the Debye temperature. A is given by $A = \Omega_0 \Gamma/\left(4\pi v_{avg}^3\right)$, where Ω_0 is the unit cell volume and Γ is the scattering parameter. The scattering parameter can be calculated by the model of Slack[45] and Abeles[46], taking $\Gamma = \Gamma_M + \Gamma_S$, where Γ_M and Γ_S are scattering parameters related to mass fluctuation and strain field fluctuation, respectively. They can be expressed as:

$$\Gamma = \Gamma_M + \Gamma_S = x(1-x)\left[\left(\frac{\Delta M}{M}\right)^2 + \varepsilon\left(\frac{\Delta a}{a}\right)^2\right] \quad , (4)$$

where ΔM and Δa are the difference in mass and lattice constants between two constituents, M and a are the molar mass and lattice constant of the alloy. The parameter ε is usually obtained by fitting experimental results. The dashed line in Fig. 7a shows the calculated thermal conductivity based on the Callaway model. The normalized lattice thermal conductivities well fall on this calculated line, proving that the mass and strain fluctuations introduced by alloying sulfur is another reason for the reduced lattice thermal conductivities observed in these solid solutions. The scattering parameters Γ_M and Γ_S, as a function of S-alloying content, are shown in Fig. S4†. For each composition, Γ_S is larger than Γ_M, which implies that the strain fluctuation contributes more to the reduction of lattice thermal conductivity than the mass fluctuation in $Cu_2Se_{1-x}S_x$.

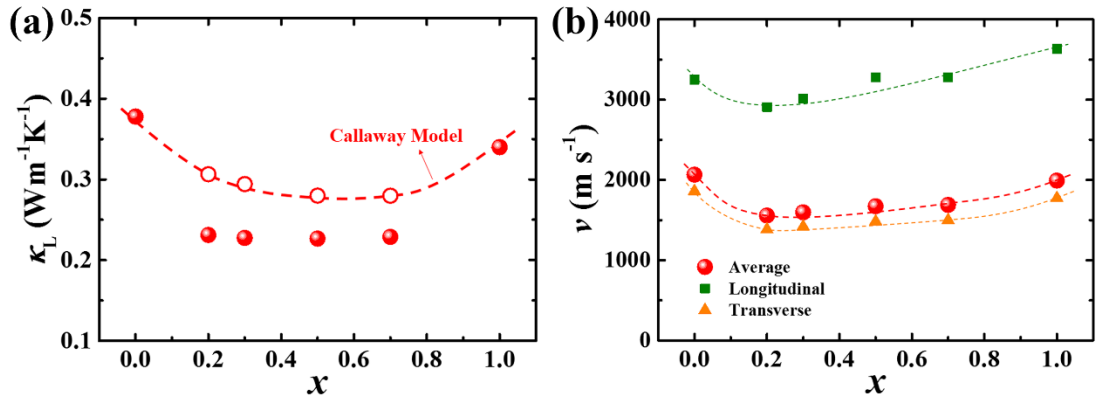

Fig. 7. Thermal transport properties of $Cu_2Se_{1-x}S_x$ (x = 0.2, 0.3, 0.5 and 0.7) as a function of sulfur content x. **(a)** Lattice thermal conductivity at 300 K. The filled circles are experimental κ_L data, and the open ones are the data calculated from normalized speed of sound using the value of Cu_2Se. The dashed line is the calculated curve by the Callaway model.[43, 44] **(b)** Longitudinal, transverse, and average speed of sound at 300 K for the $Cu_2Se_{1-x}S_x$ solid solutions. The dashed lines are guide to the eyes.

4. Conclusions

In summary, a series of $Cu_2Se_{1-x}S_x$ (x = 0.2, 0.3, 0.5, and 0.7) solid solutions have been prepared and the effects of sulfur alloying on the crystal structures and thermoelectric properties have been systematically studied. At room temperature, $Cu_2Se_{1-x}S_x$ are polymorph materials composed of varied phases with different proportions. After one or two phase transitions, all solid

solutions transform into single phase with the cubic structure. Through alloying S at the Se-sites, the hole concentrations of $Cu_2Se_{1-x}S_x$ are greatly reduced, resulting in much enhanced electrical resistivity and Seebeck coefficient. In addition, alloying S at the Se-sites also reduces the speed of sound and introduces additional point defects to scatter the phonons, leading to the extreme low thermal conductivity in $Cu_2Se_{1-x}S_x$ solid solutions. Finally, a maximum zT value of 1.65 at 950 K is achieved for $Cu_2Se_{0.8}S_{0.2}$, which is greater than those of both Cu_2Se and Cu_2S. Further performance optimization in $Cu_2Se_{1-x}S_x$ solid solutions is expected to be achieved through tuning copper vacancies to enhance their carrier concentrations.

Acknowledgements

This work was supported by National Basic Research Program of China (973-program) under Project No. 2013CB632501, National Natural Science Foundation of China (NSFC) under the No. 51472262 and 51625205, Key Research Program of Chinese Academy of Sciences (Grant No. KGZD-EW-T06), International S&T Cooperation Program of China (2015DFA51050), and Shanghai Government (16520721400 and 16XD1403900). B.B. Iverson thanks for the support by the Danish National Research Foundation (Center for Materials Crystallography, DNRF93), and the Danish Center for Synchrotron and Neutron Research (Danscatt). A. B. Blichfeld would like to thank SINO Danish Center for funding. The RIKEN SPring-8 center is acknowledged for beam time at beamline BL44B2 (RIKEN proposal No. 20150018).

Notes and references

1. G. Tan, L. D. Zhao and M. G. Kanatzidis, *Chem. Rev.*, 2016, **116**, 12123-12149.
2. G. J. Snyder and E. S. Toberer, *Nat. Mater.*, 2008, **7**, 105-114.
3. W. G. Zeier, A. Zevalkink, Z. M. Gibbs, G. Hautier, M. G. Kanatzidis and G. J. Snyder, *Angew. Chem. Int. Edit.*, 2016, **55**, 6826-6841.
4. X. Shi, L. Chen and C. Uher, *Int. Mater. Rev.*, 2016, **61**, 379-415.
5. Y. Pei, X. Shi, A. LaLonde, H. Wang, L. Chen and G. J. Snyder, *Nature*, 2011, **473**, 66-69.
6. X. Su, P. Wei, H. Li, W. Liu, Y. Yan, P. Li, C. Su, C. Xie, W. Zhao, P. Zhai, Q. Zhang, X. Tang and C. Uher, *Adv. Mater.*, 2017, DOI: 10.1002/adma.201602013.
7. T. Zhu, Y. Liu, C. Fu, J. P. Heremans, J. G. Snyder and X. Zhao, *Adv. Mater.*, 2017, **29**.
8. X. Shi and L. Chen, *Nat. Mater.*, 2016, **15**, 691-692.
9. C. Xiao, Z. Li, K. Li, P. Huang and Y. Xie, *Accounts Chem. Res.*, 2014, **47**, 1287-1295.
10. P. Qiu, X. Shi and L. Chen, *Energy Storage Mater.*, 2016, **3**, 85-97.
11. H. Liu, X. Shi, F. Xu, L. Zhang, W. Zhang, L. Chen, Q. Li, C. Uher, T. Day and G. J. Snyder, *Nat. Mater.*, 2012, **11**, 422-425.
12. Y. He, T. Day, T. Zhang, H. Liu, X. Shi, L. Chen and G. J. Snyder, *Adv. Mater.*, 2014, **26**, 3974-3978.
13. K. S. Weldert, W. G. Zeier, T. W. Day, M. Panthofer, G. J. Snyder and W. Tremel, *J. Am. Chem. Soc.*, 2014, **136**, 12035-12040.

14. S. Bhattacharya, R. Basu, R. Bhatt, S. Pitale, A. Singh, D. K. Aswal, S. K. Gupta, M. Navaneethan and Y. Hayakawa, *J. Mater. Chem. A*, 2013, **1**, 11289.
15. B. Jiang, P. Qiu, E. Eikeland, H. Chen, Q. Song, D. Ren, T. Zhang, J. Yang, B. B. Iversen and X. Shi, *J. Mater. Chem. C*, 2016, **5**, 943-952
16. Z.-H. Ge, X. Liu, D. Feng, J. Lin and J. He, *Adv. Energy Mater.*, 2016, **6**, 1600607.
17. L. L. Zhao, X. L. Wang, J. Y. Wang, Z. X. Cheng, S. X. Dou, J. Wang and L. Q. Liu, *Sci. rep.*, 2015, **5**, 7671.
18. L. Yang, Z.-G. Chen, G. Han, M. Hong, Y. Zou and J. Zou, *Nano Energy*, 2015, **16**, 367-374.
19. B. Gahtori, S. Bathula, K. Tyagi, M. Jayasimhadri, A. K. Srivastava, S. Singh, R. C. Budhani and A. Dhar, *Nano Energy*, 2015, **13**, 36-46.
20. Y. He, T. Zhang, X. Shi, S.-H. Wei and L. Chen, *NPG Asia Mater.*, 2015, **7**, e210.
21. X. Wang, P. Qiu, T. Zhang, D. Ren, L. Wu, X. Shi, J. Yang and L. Chen, *J. Mater. Chem. A*, 2015, **3**, 13662-13670.
22. A. J. Hong, L. Li, H. X. Zhu, X. H. Zhou, Q. Y. He, W. S. Liu, Z. B. Yan, J. M. Liu and Z. F. Ren, *Solid State Ionics*, 2014, **261**, 21-25.
23. P. Qiu, T. Zhang, Y. Qiu, X. Shi and L. Chen, *Energy Environ. Sci.*, 2014, **7**, 4000-4006.
24. S. Bhattacharya, A. Bohra, R. Basu, R. Bhatt, S. Ahmad, K. N. Meshram, A. K. Debnath, A. Singh, S. K. Sarkar, M. Navneethan, Y. Hayakawa, D. K. Aswal and S. K. Gupta, *J. Mater. Chem. A*, 2014, **2**, 17122-17129.
25. P. Lu, H. Liu, X. Yuan, F. Xu, X. Shi, K. Zhao, W. Qiu, W. Zhang and L. Chen, *J. Mater. Chem. A*, 2015, **3**, 6901-6908.
26. W. Qiu, P. Lu, X. Yuan, F. Xu, L. Wu, X. Ke, H. Liu, J. Yang, X. Shi, L. Chen, J. Yang and W. Zhang, *J. Chem. Phys.*, 2016, **144**, 194502.
27. D. Chakrabarti and D. Laughlin, *Bulletin of Alloy Phase Diagrams*, 1983, **4**, 254-271.
28. L. Yu, K. Luo, S. Chen and C.-G. Duan, *CrystEngComm*, 2015, **17**, 2878-2885.
29. E. Eikeland, A.B. Blichfeld, K.A. Borup, K. Zhao, J. Overgaard, X. Shi, L. Chen and B.B. Iversen, *IUCr-J*, 2017, **4**, 476.
30. A. A. Sirusi, S. Ballikaya, C. Uher and J. H. Ross, *J. Phys.Chem. C*, 2015, **119**, 20293-20298.
31. N. Vouroutzis, N. Frangis and C. Manolikas, *Phys. Status Solidi (a)*, 2005, **202**, 271-280.
32. L. Zhao, X. Wang, F. Y. Fei, J. Wang, Z. Cheng, S. Dou, J. Wang and G. J. Snyder, *J. Mater. Chem. A*, 2015, **3**, 9432-9437.
33. X. Su, F. Fu, Y. Yan, G. Zheng, T. Liang, Q. Zhang, X. Cheng, D. Yang, H. Chi, X. Tang, Q. Zhang and C. Uher, *Nat. Commun.*, 2014, **5**, 4908.
34. K. Zhao, A. B. Blichfeld, H. Chen, Q. Song, T. Zhang, C. Zhu, D. Ren, R. Hanus, P. Qiu, B. B. Iversen, F. Xu, G. J. Snyder, X. Shi and L. Chen, *Chemistry of Materials*, 2017, DOI: 10.1021/acs.chemmater.7b01687.
35. Y. He, P. Lu, X. Shi, F. Xu, T. Zhang, G. J. Snyder, C. Uher and L. Chen, *Adv. Mater.*, 2015, **27**, 3639-3644.
36. K. Zhao, P. Qiu, Q, Song, A. Blichfeld, E. Eikeland, D. Ren, B. Ge, B. Iversen, X. Shi and L. Chen, *Mater. Tod. Phy.*, 2017, **1**, 14.
37. K. Kato and H. Tanaka, *Adv. Phys.: X*, 2016, **1**, 55-80.
38. C. Frondel and U. B. Marvin, Nature, 1967, **214**, 587-589.
39. M. Oliveria, R. McMullan and B. Wuensch, *Solid State Ionics*, 1988, **28**, 1332-1337.
40. S. Johnsen, J. He, J. Androulakis, V. P. Dravid, I. Todorov, D. Y. Chung and M. G. Kanatzidis,

J. Am. Chem. Soc., 2011, **133**, 3460-3470.

41. A. F. May, J.-P. Fleurial and G. J. Snyder, *Phys. Rev. B*, 2008, **78**.
42. T. W. Day, K. A. Borup, T. Zhang, F. Drymiotis, D. R. Brown, X. Shi, L. Chen, B. B. Iversen and G. J. Snyder, *Mater. Renewable Sustainable Energy*, 2014, **3**, 26.
43. J. Callaway, *Phys. Rev.*, 1959, **113**, 1046.
44. J. Callaway and H. C. von Baeyer, *Phys. Rev.*, 1960, **120**, 1149.
45. G. A. Slack, *Phys. Rev.*, 1957, **105**, 829.
46. B. Abeles, *Phys. Rev.*, 1963, **131**, 1906.